A SEARCH FOR SUPERSYMMETRY IN EVENTS WITH A Z BOSON, JETS, AND MISSING TRANSVERSE ENERGY IN $p-p$ COLLISIONS WITH $\sqrt{s}=13$ TEV WITH THE ATLAS DETECTOR

TOVA RAY HOLMES

Physics Department
University of California, Berkeley

August 2016 – version 1.0

ABSTRACT

PUBLICATIONS

Some ideas and figures have appeared previously in the following publications:

Put your publications from the thesis here. The packages `multibib` or `bibtopic` etc. can be used to handle multiple different bibliographies in your document.

ACKNOWLEDGEMENTS

Put your acknowledgements here.

CONTENTS

LIST OF FIGURES

LIST OF TABLES

LISTINGS

[September 12, 2016 at 11:59 – classicthesis version 1.0]

ACRONYMS

LHC   Large Hadron Collider

IBL   Insertable B-Layer

MS   Muon Spectrometer

ID   Inner Detector

SCT   Silicon Microstrip Tracker

TRT   Transition Radiation Tracker

NN   Neural Network

CCA   Connected Component Analysis

ToT   Time Over Threshold

MC   Monte Carlo simulation

SM   Standard Model

Part I

INTRODUCTION

The centerpiece of this thesis is a search for Supersymmetry, but it also includes all the scaffolding and background necessary to understand the search. An overview of the Large Hadron Collider (LHC) and the ATLAS Detector are presented along with the theory that motivates the search.

INTRODUCTION

The pages that follow detail the author's work on the ATLAS experiment from 2011 through 2016, focusing on an analysis of 13TeV proton-proton collisions at the LHC looking for Supersymmetry with the ATLAS Detector.

CHAPTER 2 outlines the Standard Model of Particle Physics and the benefits of extending it to include Supersymmetry, then continues to describe the motivation behind searching for this particular model.

CHAPTER 3 describes the LHC and its operation.

CHAPTER 4 contains descriptions of the many pieces of the ATLAS detector, and how they serve to detect particles coming from LHC collisions.

CHAPTER 5 presents a neural network designed to improve tracking in the ATLAS Pixel Detector, and describes the benefits of its implementation.

Part II

THEORY AND MOTIVATION

This section describes the theoretical foundation for the analysis presented in Part iv. It includes an overview of the Standard Model, including its phenomenology in a $p - p$ collider. The theory of Supersymmetry is explained, and the motivation for extending the Standard Model to include it is presented. In addition, this section includes an explanation of Monte Carlo generators and details about the specific form of Supersymmetry searched for in this analysis.

2

THEORY AND MOTIVATION

This chapter describes the Standard Model of particle physics and its phenomenology in proton-proton collisions at the LHC. The shortcomings of the Standard Model are discussed, and Supersymmetry is presented as a possibile solution to many of these shortcomings. Additionally, the simplified Supersymmetric models to be used in the analysis discussed in Part iv are introduced. Lastly, Monte Carlo generators, which are used make phenomenological predictions from these models, are described.

2.1 THE STANDARD MODEL

The Standard Model (SM) of particle physics describes the interactions of all of the particles currently known to exist, and consists of both matter particles and force carriers. This model has been unprecidentedly successful in predicting new particles and phenomena, including the prediction of the Higgs particle almost 50 years before its discovery in 2012, which completed the SM. This section describes the components of the SM and how they interact, focusing on the environment of the LHC.

The SM is a non-abelian gauge theory blah blah blah
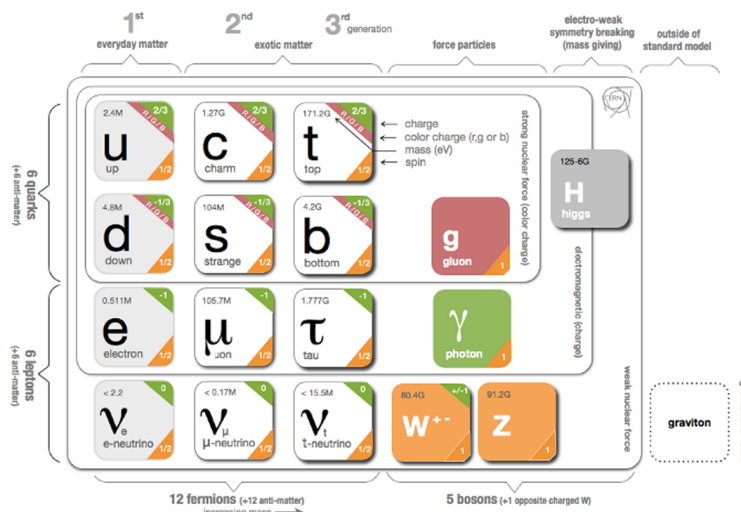
Figure 1: The Standard Model of particle physics. [17]

2.1.1 *Matter*

The matter described by the SM is made up of fermions, spin-$\frac{1}{2}$ particles which can be broken into two groups, quarks and leptons.

2.1.1.1 *Leptons*

2.1.1.2 *Quarks*

2.1.2 *Forces*

2.1.3 *The Higgs Particle*

2.1.4 *Phenomenology of Proton-Proton Collisions*

2.1.4.1 *Parton Distribution Functions*

2.1.5 *Problems in the Standard Model*

2.2 SUPERSYMMETRY

2.2.1 *Supersymmetry Phenomenology*

2.2.2 *Solutions to Standard Model Problems*

2.2.3 *Supersymmetry Signatures in* $p-p$ *Collisions*

2.2.3.1 *Simplified Models Used in This Analysis*

2.3 MONTE CARLO GENERATORS

Part III

THE EXPERIMENT

This section describes the LHC and the ATLAS detector, which collectively provide the physical environment and the data collection for the analysis discussed in Part iv.

THE LARGE HADRON COLLIDER

The LHC is unique in the world, producing proton-proton collisions at energies an order of magnitude higher than any accelerator before. It provides unique environments at its collision points where massive, unstable particles can exist for an instant, then decay to the ordinary material of the universe. It is the goal of the ATLAS experiment to identify these short-lived particles, but LHC's work of producing them is equally complex.

3.1 OPERATION OF THE LARGE HADRON COLLIDER

THE ATLAS DETECTOR

The ATLAS detector circumscribes the LHC's beam pipe, enclosing the collision point with a series of particle detecting layers, aimed at making as many measurements of the particles leaving the collision point as possible. Its goal is to get a precise measurement of all the stable or semi-stable particles flying from proton-proton collisions at its center, allowing analyzers to fully reconstruct the kinematics of the underlying processes.

The ATLAS detector is the largest detector of its kind, measuring 44 m in length and 25 m in height, as seen in Figure 2. The size is mainly determined by the constraints of the Muon Spectrometer (MS), discussed in Section 4.4, which is the largest and outermost subsystem. The MS is submerged in a spatially varying magnetic field provided by three toroidal magnets, while the Inner Detector (ID) (Section 4.2) is encased by a superconducting solenoid, which provides a uniform 2 T field throughout its volume [1].
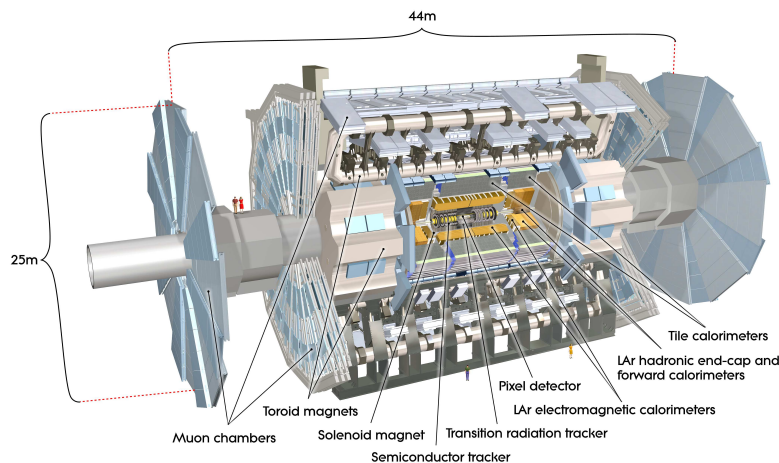
Figure 2: Diagram of the ATLAS detector, with subsystems and magnets identified.

4.1 COORDINATE SYSTEM USED IN THE ATLAS DETECTOR

The ATLAS detector is centered around a the collision point in the beam pipe, and is built radially out from the pipe, maintaining as much rotational symmetry as possible. It is also symmetric in the forward-backward directions. Because of this geometry, a coordinate system using the collision point as the origin is used, with the beam

13

pipe defining the z-axis. The positive x direction is defined as pointing to the center of the LHC ring, while the positive y direction points upwards. For ease of reference, the side of the detector in the positive-z direction is referred to as the A side, and the other side is referred to as the C side.

Because of the radial design of the detector, angular coordinates are often used. The azimuthal angle ϕ defines the radial distance around the beam pipe and the polar angle θ defines the angle from the beam axis (z). However, a transformation of the polar angle called pseudorapidity (η) is used more often, and is defined as

$$\eta = -\ln[\tan\frac{\theta}{2}]. \tag{1}$$

Building on this variable definition, distance between objects is typically defined as

$$\Delta R = \sqrt{\Delta\eta^2 + \Delta\phi^2}. \tag{2}$$

Often variables are defined purely in the transverse plane, which is indicated by a subscripted T, as in p_T, which gives an object's transverse momentum. Another common usage is E_T^{miss}, which gives the negative vectorial sum of the energy in an event.

4.2   THE INNER DETECTOR

One goal of the ATLAS detector is to produce tracks, predictions of the paths particles take as they travel through the detector. Collisions in the detector produce about 1000 particles, so identifying and differentiating all these tracks is both a hardware and a computational challenge. The ID, also called the Tracker, is responsible for providing high enough resolution measurements that each of these tracks and its precise position can be recorded. This tracking system consists of three subdetectors which each produce electrical responses to charged particles passing through their active material. Each of these signals is called a hit. ATLAS tracking software considers all these hits and forms tracks, with the goal of minimizing fake tracks due to random noise. Some details of this process is discussed at length in Chapter 6. The full ID can be seen in Figure 3, while a schematic in Figure 4 demonstrates the η coverage of each detector.

4.2.1   *The Pixel Detector*

The Pixel detector lies closest to the beam pipe of the LHC, and has four layers comprising 92 million read-out channels. There are three
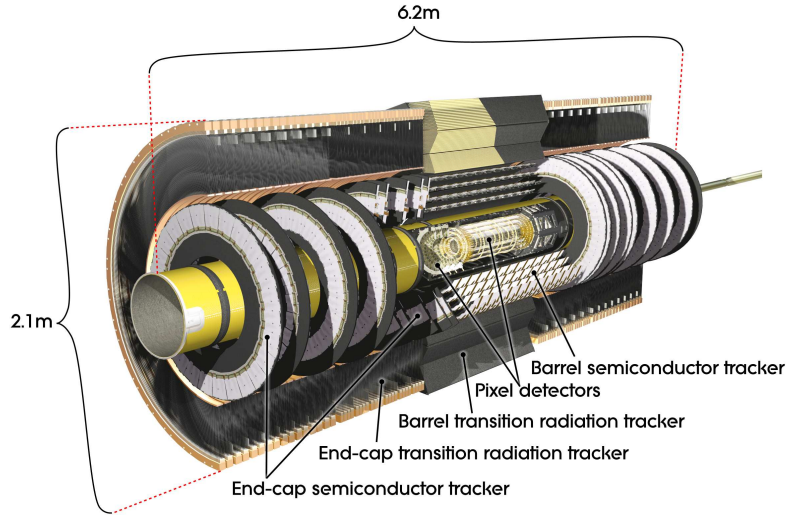
Figure 3: Diagram of the ATLAS Inner Detector, containing the Pixel, SCT, and TRT subsystems.

standard layers, referred to as Layers 1-3 (L1, L2, L3), and an additional layer added for the 2015 data-taking, called the Insertable B-Layer (IBL).

4.2.1.1 *The Original Pixel Detector*

The Pixel Detector consists of high-precision silicon chip pixel sensors, with 1744 sensors total. Each sensor is identical, containing 47232 pixels, which are typically each 50×400 μm^2.

As shown in Figure 4, the central η region (barrel) is covered by three concentric cylindrical layers of sensors, while the higher η region (endcap) is covered by a series of three disks positioned in the $x - y$ plane. Together, they give complete coverage out to η = 2.5, and a particle coming from the collision point will typically by measured by three layers. Each of these measurements is accurate in the barrel (endcap) to 10 μm in the $R - \phi$ direction and 115 μm in the z (R) direction.

4.2.1.2 *Addition of the IBL*

In 2015, the IBL was lowered into the ATLAS cavern and added to the Pixel Detector. This layer sits on top of the beam pipe, inside barrel L1, which was formerly responsible for the first measurement of charged particles coming from a collision. TODO: add info about precision

As the IBL's' name suggests, it was added to improve detection of B mesons, whose non-trivial lifetimes create secondary vertices in ATLAS events, which allow them to be distinguished from other particles with precise track measurement. The IBL is closer to the interaction point and has a smaller resolution, giving it a better chance to see these slightly displaced vertices.
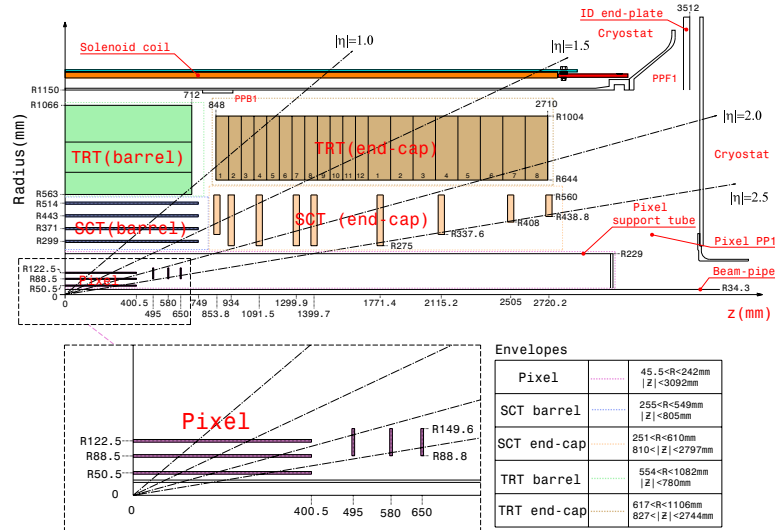
Figure 4: Diagram of one-quarter of the ATLAS Inner Detector, with lines drawn to indicate various η locations. The labels PP1, PPB1 and PPF1 indicate the patch-panels for the ID services. TODO: what is that.

4.2.2 *The Silicon Microstrip Tracker*

The Silicon Microstrip Tracker (SCT) employs similar technology to the Pixel Detector, with 15912 sensors and 6.3 million readout channels. Its difference from the Pixel Detector is in the readout, which is performed by a series of 12 cm long strips with a width of 80 μm. These layers are paired, placed on top of one another at a small (40 mrad) angle to allow for position determination in both directions, giving 4 spatial measurements for each particle passing through the SCT. In the barrel, these strips run parallel to the beam pipe, while in the endcap, they are arranged radially. These strips have a resolution in the barrel (endcap) of 17 μm in the $R - \phi$ direction and 580 μm in the z (R) direction.

4.2.3 *The Transition Radiation Tracker*

The Transition Radiation Tracker (TRT) uses 4mm diameter gas-filled tubes, each with a high voltage wire suspended along the center of the tube. The tubes run the length of the barrel, with a separate wire in the positive and negative z direction. In the endcap, the tubes are arranged radially. In total, there are about 351,000 readout channels in the TRT. This detector makes measurements only in the $R - \phi$ direction, where the resolution of each measurement is 130 μm. Each particle typically creates about 36 hits as it passes through the TRT.

TODO is any of this right? Particles passing through the gas mixture of the TRT ionize the gas, producing electrons which drift towards

the wire due to a potential difference applied between it and the straw. This process takes about 48 ns, and the signal can be directly read out, giving the fastest measurement of particles in the ID. This speedy readout is essential to triggering, discussed more in Section 4.6.

The TRT also responds to low-energy transition radiation photons, which produce a much larger signal than charged particles passing through the detector. Because of this strong difference in signals, hits from the TRT are used to help differentiate between electrons and photons in the detector.

4.3 THE CALORIMETERS

Unlike the tracking detectors, which aim to take measurements of a particle with minimal alterations of its trajectory, the calorimeters measure the the energy of objects by stopping them entirely. The calorimeters, which can be seen in Figure 5, provide coverage out to $\eta < 4.9$. Higher granularity electromagnetic measurements are made within $|\eta| < 2.5$, where the ID provides tracking capability, in order to give precision measurements of the energy of photons and electrons, and provide reduced resolution measurements at higher η. The hadronic calorimeters provides coarser granularity, which is sufficient to determine the energy of jets.
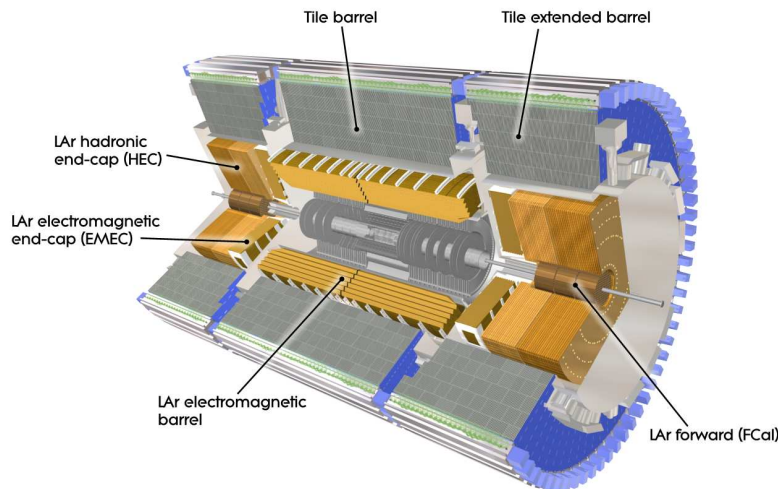
Figure 5: The calorimeter system of the ATLAS detector.

TODO make sure jets are in theory.

Another task of the calorimeter system is to limit punch-through to the MS, described in Section 4.4. All other particles must be fully stopped by the calorimeters to allow for clean signals from muons, and to measure the total energy of the particle. This requirement sets minimum sizes for each of the calorimeters.

THE LAR ELECTROMAGNETIC CALORIMETER   uses liquid argon as its active detector medium alternating with layers of lead acting as the absorber. The layers are shaped like accordions, which allows for complete coverage with multiple layers of active material, three in central η ($0 < |\eta| < 2.5$) and two at higher η ($2.5 < |\eta| < 3.2$). At $|\eta| < 1.8$, an instrumented liquid argon presampler provides a measurement of energy lost prior to reaching the calorimeters.

THE TILE CALORIMETER   is a hadronic calorimeter which surrounds the LAr Calorimeter. It uses layers of steel as its absorber with scintillating tiles as the active material between them, which are read out by photomultiplier tubes. The Tile Calorimeter covers $|\eta| < 1.7$.

THE LAR HADRONIC ENDCAP CALORIMETER   covers the hadronic calorimetery for higher η. It uses liquid argon active material and copper plate absorbers. This calorimeter covers $1.5 < |\eta| < 3.2$, overlapping with the hadronic calorimeters in either direction of its η range.

THE FCAL   or forward calorimeter provides electromagnetic and hadronic coverage at very high η ($3.1 < |\eta| < 4.9$). This calorimeter also uses liquid argon as its active material, and uses copper-tungsten as the absorber.

4.4   THE MUON SPECTROMETER

4.5   THE MAGNET SYSTEM

4.6   THE TRIGGER SYSTEM

OBJECT RECONSTRUCTION IN THE ATLAS DETECTOR

APPLICATION OF A NEURAL NETWORK TO PIXEL CLUSTERING

6.1 CLUSTERING IN THE PIXEL DETECTOR

Creating tracks from individual hits in the Inner Detector is one of most computationally challenging parts of the reconstruction of AT-LAS events. Each event typically contains thousands of hits in the pixel detector alone, which must be combined into one coherent picture of which particles traversed the detector, and how they moved and lost energy as they traveled. A typical particle deposits charge in several pixels per layer, forming a series of clusters which can be connected together to form a track. This track can in turn be used to measure the charge, momentum, and trajectory of the particle, and in many cases, provides ATLAS's most precise measurement of a charged particle.
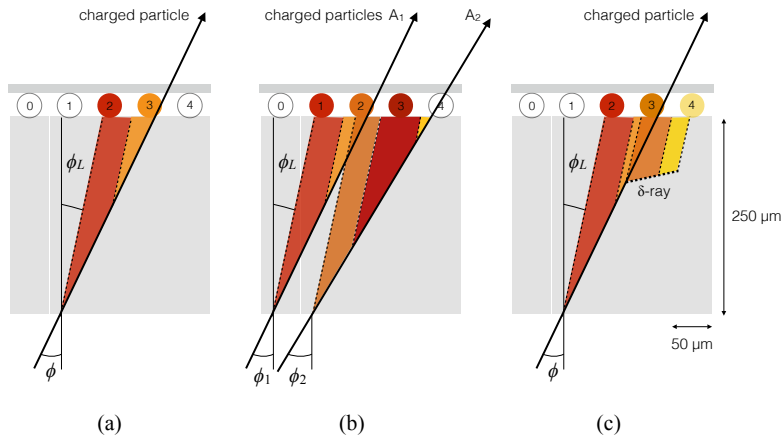
Figure 6: A few possible types of clusters in the Pixel Detector. (a) shows a single particle passing through a layer of the detector, (b) shows two particles passing through the detector, creating a single merged cluster, and (b) shows a single particle emitting a δ-ray as it passes through the detector.

The process of going from clusters to track is relatively simple in an isolated environment in which one particle travels cleanly through all the layers, but can be complicated by multiple close-by tracks and by a single particle's emission of low energy particles, called δ-rays. In these cases, it can be hard to tell how many particles were involved in creating a cluster, and where exactly each of those particles passed through the layer. A few examples of these cases can be seen in Fig-

ure 6 . The process of determining this is called Clustering, and it has recently been updated from a charge interpolation method to a method using a NN.

6.1.1 *Charge Interpolation Method*

A typical cluster contains a few pixel hits spanning in the x and y directions, each with its own measurement of charge deposition, or Time Over Threshold (ToT). The extent of the cluster is defined by grouping together any pixels with a shared edge or corner. In the charge interpolation method, also called the CCA clustering algorithm, these individual hits are combined to make one estimation of the position a single particle which passed through them, using the following equation:

$$x_{cluster} = x_{center} + \Delta_x(\phi, N_{row}) \cdot \left[\Omega_x - \frac{1}{2} \right] \tag{3}$$

$$x_{cluster} = x_{center} + \Delta_x(\phi, N_{row}) \cdot \left[\Omega_x - \frac{1}{2} \right] \tag{4}$$

where $\Omega_{x(y)}$ is defined by

$$\Omega_{x(y)} = \frac{q_{last\ row(col)}}{q_{first\ row(col)} + q_{last\ row(col)}} \tag{5}$$

and q represents the ToT of a given pixel, and $\Delta_{x(y)}$ is a function derived from either data or Monte Carlo simulation (MC) and produces an output related to the projected length of the particles track on the pixel sensor and is measured as a function of ϕ, the incident angle of a particle on the sensor, and $N_{row(col)}$, the number of pixels in the x and y direction.

In a simple case, such as (a) of Figure 6 , this method works quite effectively. However, in cases like (b), it has no ability distinguish two-particle from one-particle clusters, and can only assign a cluster center between the two particles' locations, despite that intermediate pixel having the lowest ToT. Furthermore, because this method can't differentiate two-particle clusters, the tracking software can't use that information to preferentially allow multiple tracks to be fit to the cluster. In cases like (c), the δ-ray will bias the measurement of the particle's position in whichever direction it is emitted.

6.1.2 *Improving Measurement with Neural Networks*

To address these problems, a series of NNs were created [2]. The first determines the number of particles in a given cluster, the second predicts their positions with the cluster, and the third assesses the resolution of the position measurement.

These NNs are all trained with:

- a 7×7 grid of cluster ToT information[1]

- a seven-element vector containing the y-size of the pixels in the grid

- the layer number of the cluster

- a variable indicating whether the cluster located in the barrel or endcap

- θ and ϕ variables projecting the incident angles of the particle on the sensor, assuming it comes from the interaction point

- the η index of the pixel module

After the Number NN predicts a number of particles associated with the cluster, required to be between 1 and 3, the same inputs are fed to one of three Position NNs based on the determined number of particles, which then outputs the x and y positions of each of the particles. Then, the same inputs combined with the output of the Position NN are fed into one of three Error NNs (also distinguished by number of particles), which outputs a resolution for each of the position predictions made. An example of the output of this process can be seen in Figure 7, where the improved position resolution from the ability to identify a multi-particle cluster is evident. The particle location predictions from the NNs are then handed to the tracking software, which is able to independently consider multiple locations from a given cluster to find the best fit.

6.2 IMPACT OF THE NEURAL NETWORK

The NN was first applied to 7TeV data, where it improved position resolution for particles in small and large clusters. Figure 8 shows the improvement from the addition of the NN in x resolution in different cluster sizes. The improvement from CCA clustering is particularly evident in the 4-pixel case, where the double peaked structure of the interpolation method has been completely removed with the NN.

6.2.1 *The Neural Network in 13 TeV Data*

In Run 2, tracking algorithm is first run on the CCA clusters, where it constructs loose tracks that allow shared clusters, clusters to which multiple tracks are fit. The NN is then used to identify which clusters are likely to have had multiple particles pass through them, and to identify the positions of those particles. In the case that the cluster is

---

1 Clusters spanning more than seven pixels in either direction are split into multiple clusters.
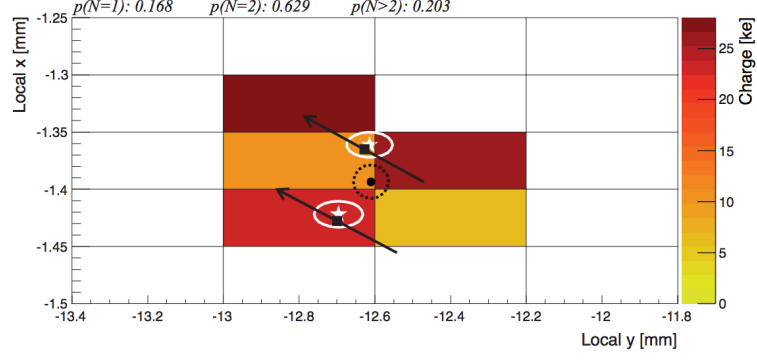
Figure 7: One example of a two-particle cluster and its truth information compared with the output of the NNs. At top, the $p(N = i)$ values give the output of the Number NN, the probabilities that the cluster contains 1, 2, and 3 particles. Given the highest probability is for $N = 2$, the other NNs predict the postion and errors of the two particles (in white). The black arrows and squares represent the truth information from the cluster, and the black dot and dotted line show the position measurement for the un-split cluster.
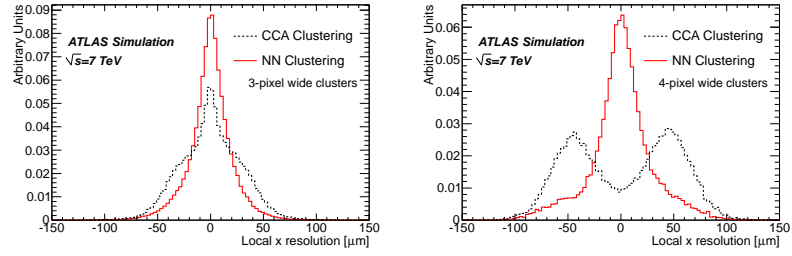
Figure 8: x resolutions for clusters with 3 (left) and 4 (right) pixels in the x direction in 7TeV data for CCA and NN clustering.

determined to have resulted only from one particle, tracks that share that cluster are penalized.

Performance in 13 TeV [3].

Robustness [4]

Part IV

SEARCHING FOR SUPERSYMMETRY

This section describes an analysis of the ATLAS data carried out by the author and her analysis team. The analysis was performed on events from $p-p$ collisions provided by the LHC at $\sqrt{s}$=13 TeV. It searches for events like those described in Section 2.2.3.1, which contain a Z boson decaying to leptons, jets, and missing transverse energy. The selection of a signal region in which to search for these events, background estimates, systematic uncertainty estimates, results, and interpretations are all discussed.

BACKGROUND PROCESSES

This analysis is fundamentally a search for Supersymmetry in events with two leptons whose invariant mass is consistent with a Z boson. Additional event selections are made to reduce Standard Model processes relative to potential Supersymmetric processes, defined by simplified models discussed in Section 2.2.3.1. Supersymmetric events typically have large amounts of E_T^{miss}, H_T (the scalar sum of the p_T of objects in the event), and many jets. All of these features can help isolate these events from backgrounds. To understand what cuts would optimize the sensitivity of the search, it is essential to first understand what these Standard Model backgrounds are.
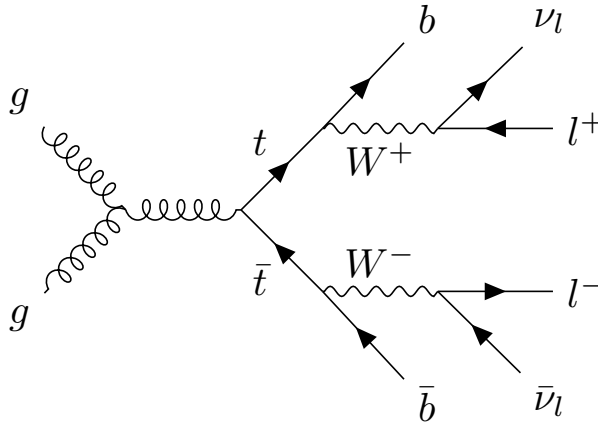
Figure 9: An example Feynman diagram of $t\bar{t}$ production and decay.

$t\bar{t}$ is the largest background for this search. Figure 9 shows an example of this process, which can decay to many jets, leptons, and neutrinos, which are seen in the detector as E_T^{miss}. Thus, $t\bar{t}$ naturally has high E_T^{miss} and H_T, jets, and leptons from two different W boson decays, which may coincidentally form an invariant mass on the Z peak. These events are very difficult to separate from potential signals, though keeping the mass window small and increasing E_T^{miss} and H_T above the typical values for $t\bar{t}$ events can help reduce them.

DIBOSON production is the next leading background. These events can contain real Z bosons and will peak on-Z like a signal. In addition, in events like Figure 10, an additional W boson can decay to another lepton and a neutrino, providing E_T^{miss}. The pictured process can occur with associated jets, but at reduced rates, so adding a jet requirement to the signal region can help reduce these events. If the
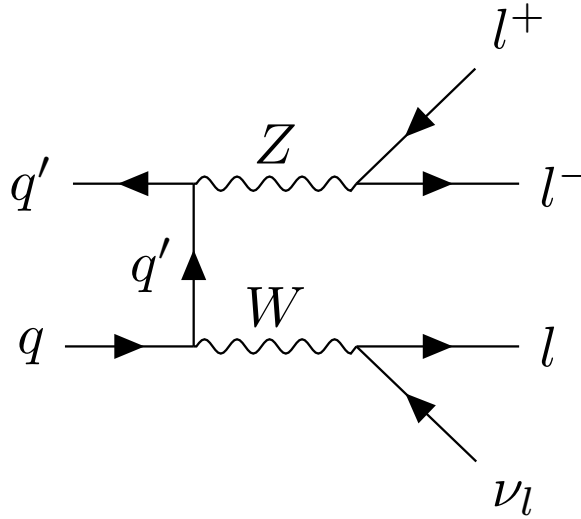
Figure 10: An example Feynman diagram of the production and decay of a WZ event.

W boson in this diagram instead decayed to two jets, there would be no true E_T^{miss} from a neutrino, so a E_T^{miss} cut in conjunction with a jet cut is very effective in reducing the total diboson background.
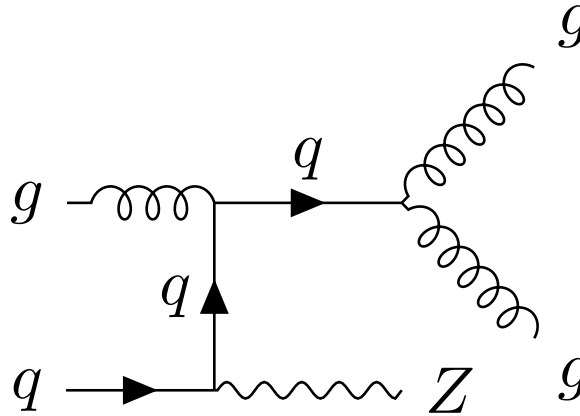
Figure 11: An example Feynman diagram of the production and decay of a $Z/\gamma^* + $ jets event.

$Z/\gamma^* + $ JETS   processes are very common but, as shown in Figure 11, don't produce any true E_T^{miss} or a very large number of jets. Thus a high H_T cut can help reduce this background, but a E_T^{miss} cut is the most powerful. Events with very mismeasured jets or leptons can fake high E_T^{miss}, but these drastic mismeasurements are rare.

Other processes can contribute to the Standard Model background at lower rates. Processes similar to $Z/\gamma^* + $ jets but with a W boson instead of a Z have real E_T^{miss} from leptonic W decays, but only one

lepton. However, a fake or non-prompt lepton can cause these events to look very similar to simulated signals. Additionally, there are rare processes such as $t\bar{t}$ in association with bosons that will also be difficult to separate from signal processes.

7.1 MONTE CARLO SAMPLES

To precisely compare simulated signal to backgrounds, MC samples are generated for each of these processes. Table 1 details the method used to produce each sample. With these and the simulated background, optimizations on a signal regioin can be made to maximize potential for discovery or exclusion of simplified Supersymmetric models. These comparisons and the signal region definition can be found in Section 9.1.

Physics process	Generator		Parton Shower	Cross section	Tune	PDF set
$t\bar{t} + W$ and $t\bar{t} + Z$ [5, 18]	MG5_aMC@NLO		Pythia 8.186	NLO [11, 20]	A14	NNPDF23LO
$t\bar{t} + WW$ [5]	MG5_aMC@NLO		Pythia 8.186	LO [9]	A14	NNPDF23LO
$t\bar{t}$ [8]	Powheg Box v2 r3026		Pythia 6.428	NNLO+NNLL [15, 16]	Perugia2012	NLO CT10
Single-top (Wt) [8]	Powheg Box v2 r2856		Pythia 6.428	Approx. NNLO [19]	Perugia2012	NLO CT10
WW,	Sherpa 2.1.1		Sherpa 2.1.1	NNLO [10, 12]	Sherpa default	NLO CT10
WZ and ZZ [7]	Sherpa 2.1.1		Sherpa 2.1.1	NNLO [10, 12]	Sherpa default	NLO CT10
$Z/\gamma^*(\to \ell\ell)$ + jets [6]	Sherpa 2.1.1		Sherpa 2.1.1	NNLO [13, 14]	Sherpa default	NLO CT10

Table 1: Simulated background event samples used in this analysis with the corresponding matrix element and parton shower generators, cross-section order in α_s used to normalise the event yield, underlying-event tune and PDF set.

8

OBJECT IDENTIFICATION AND SELECTION

8.1 ELECTRONS

8.2 MUONS

8.3 JETS

8.4 PHOTONS

9

EVENT SELECTION

9.1 SIGNAL REGION

9.2 CONTROL AND VALIDATION REGIONS

10

BACKGROUND ESTIMATION

10.1 FLAVOR SYMMETRIC PROCESSES

10.2 $Z/\gamma^* + $ JETS BACKGROUND

10.3 FAKES

10.4 DIBOSONS

10.5 OTHER RARE PROCESSES

35

SYSTEMATIC UNCERTAINTY

12

RESULTS

13

INTERPRETATIONS

Part V

CONCLUSIONS

This section presents conclusions and an outlook for future work.

14

CONCLUSIONS

15

OUTLOOK

Part VI

APPENDIX

APPENDIX TEST

Aliquam lectus. Vivamus leo. Quisque ornare tellus ullamcorper nulla. Mauris porttitor pharetra tortor. Sed fringilla justo sed mauris. Mauris tellus. Sed non leo. Nullam elementum, magna in cursus sodales, augue est scelerisque sapien, venenatis congue nulla arcu et pede. Ut suscipit enim vel sapien. Donec congue. Maecenas urna mi, suscipit in, placerat ut, vestibulum ut, massa. Fusce ultrices nulla et nisl.

Etiam ac leo a risus tristique nonummy. Donec dignissim tincidunt nulla. Vestibulum rhoncus molestie odio. Sed lobortis, justo et pretium lobortis, mauris turpis condimentum augue, nec ultricies nibh arcu pretium enim. Nunc purus neque, placerat id, imperdiet sed, pellentesque nec, nisl. Vestibulum imperdiet neque non sem accumsan laoreet. In hac habitasse platea dictumst. Etiam condimentum facilisis libero. Suspendisse in elit quis nisl aliquam dapibus. Pellentesque auctor sapien. Sed egestas sapien nec lectus. Pellentesque vel dui vel neque bibendum viverra. Aliquam porttitor nisl nec pede. Proin mattis libero vel turpis. Donec rutrum mauris et libero. Proin euismod porta felis. Nam lobortis, metus quis elementum commodo, nunc lectus elementum mauris, eget vulputate ligula tellus eu neque. Vivamus eu dolor.

A.1 APPENDIX SECTION TEST

Nulla in ipsum. Praesent eros nulla, congue vitae, euismod ut, commodo a, wisi. Pellentesque habitant morbi tristique senectus et netus et malesuada fames ac turpis egestas. Aenean nonummy magna non leo. Sed felis erat, ullamcorper in, dictum non, ultricies ut, lectus. Proin vel arcu a odio lobortis euismod. Vestibulum ante ipsum primis in faucibus orci luctus et ultrices posuere cubilia Curae; Proin ut est. Aliquam odio. Pellentesque massa turpis, cursus eu, euismod nec, tempor congue, nulla. Duis viverra gravida mauris. Cras tincidunt. Curabitur eros ligula, varius ut, pulvinar in, cursus faucibus, augue.

More dummy text

Nulla mattis luctus nulla. Duis commodo velit at leo. Aliquam vulputate magna et leo. Nam vestibulum ullamcorper leo. Vestibulum condimentum rutrum mauris. Donec id mauris. Morbi molestie justo et pede. Vivamus eget turpis sed nisl cursus tempor. Curabitur mollis sapien condimentum nunc. In wisi nisl, malesuada at, dignissim sit amet, lobortis in, odio. Aenean consequat arcu a ante. Pellentesque porta elit sit amet orci. Etiam at turpis nec elit ultricies imperdiet. Nulla facilisi. In hac habitasse platea dictumst. Suspendisse

LABITUR BONORUM PRI NO	QUE VISTA	HUMAN
fastidii ea ius	germano	demonstratea
suscipit instructior	titulo	personas
quaestio philosophia	facto	demonstrated

Table 2: Autem usu id.

viverra aliquam risus. Nullam pede justo, molestie nonummy, scelerisque eu, facilisis vel, arcu.

A.2   ANOTHER APPENDIX SECTION TEST

Curabitur tellus magna, porttitor a, commodo a, commodo in, tortor. Donec interdum. Praesent scelerisque. Maecenas posuere sodales odio. Vivamus metus lacus, varius quis, imperdiet quis, rhoncus a, turpis. Etiam ligula arcu, elementum a, venenatis quis, sollicitudin sed, metus. Donec nunc pede, tincidunt in, venenatis vitae, faucibus vel, nibh. Pellentesque wisi. Nullam malesuada. Morbi ut tellus ut pede tincidunt porta. Lorem ipsum dolor sit amet, consectetuer adipiscing elit. Etiam congue neque id dolor.

Donec et nisl at wisi luctus bibendum. Nam interdum tellus ac libero. Sed sem justo, laoreet vitae, fringilla at, adipiscing ut, nibh. Maecenas non sem quis tortor eleifend fermentum. Etiam id tortor ac mauris porta vulputate. Integer porta neque vitae massa. Maecenas tempus libero a libero posuere dictum. Vestibulum ante ipsum primis in faucibus orci luctus et ultrices posuere cubilia Curae; Aenean quis mauris sed elit commodo placerat. Class aptent taciti sociosqu ad litora torquent per conubia nostra, per inceptos hymenaeos. Vivamus rhoncus tincidunt libero. Etiam elementum pretium justo. Vivamus est. Morbi a tellus eget pede tristique commodo. Nulla nisl. Vestibulum sed nisl eu sapien cursus rutrum.

There is also a useless Pascal listing below: Listing 1.

Listing 1: A floating example (`listings` manual)

```
1  for i:=maxint downto 0 do
   begin
   { do nothing }
   end;
```

BIBLIOGRAPHY

[1] ATLAS Collaboration. "The ATLAS Experiment at the CERN Large Hadron Collider." In: *JINST* 3 (2008), S08003. DOI: 10 . 1088/1748-0221/3/08/S08003.

[2] ATLAS Collaboration. "A neural network clustering algorithm for the ATLAS silicon pixel detector." In: *JINST* 9 (2014), P09009. DOI: 10 . 1088 / 1748 - 0221 / 9 / 09 / P09009. arXiv: 1406 . 7690 [hep-ex].

[3] ATLAS Collaboration. *Measurement of performance of the pixel neural network clustering algorithm of the ATLAS experiment at* $\sqrt{s}$ = 13 *TeV*. ATL-PHYS-PUB-2015-044. 2015. URL: http://cdsweb.cern.ch/record/2054921.

[4] ATLAS Collaboration. *Robustness of the Artificial Neural Network Clustering Algorithm of the ATLAS experiment*. ATL-PHYS-PUB-2015-052. 2015. URL: http://cdsweb.cern.ch/record/2116350.

[5] ATLAS Collaboration. *Modelling of the* t$\bar{t}$H *and* t$\bar{t}$V (V = W, Z) *processes for* $\sqrt{s}$ = 13 *TeV ATLAS analyses*. ATL-PHYS-PUB-2016-005. 2016. URL: http://cds.cern.ch/record/2120826.

[6] ATLAS Collaboration. *Monte Carlo Generators for the Production of a W or* Z/γ^* *Boson in Association with Jets at ATLAS in Run 2*. ATL-PHYS-PUB-2016-003. 2016. URL: http://cds.cern.ch/record/2120133.

[7] ATLAS Collaboration. *Multi-Boson Simulation for 13 TeV ATLAS Analyses*. ATL-PHYS-PUB-2016-002. 2016. URL: http : / / cds . cern.ch/record/2119986.

[8] ATLAS Collaboration. *Simulation of top quark production for the ATLAS experiment at* $\sqrt{s}$ = 13 *TeV*. ATL-PHYS-PUB-2016-004. 2016. URL: http://cds.cern.ch/record/2120417.

[9] J. Alwall, R. Frederix, S. Frixione, V. Hirschi, F. Maltoni, O. Mattelaer, H. S. Shao, T. Stelzer, P. Torrielli, and M. Zaro. "The automated computation of tree-level and next-to-leading order differential cross sections, and their matching to parton shower simulations." In: *JHEP* 07 (2014), p. 079. DOI: 10.1007/JHEP07(2014)079. arXiv: 1405.0301 [hep-ph].

[10] J. M. Campbell and R. K. Ellis. "An update on vector boson pair production at hadron colliders." In: *Phys. Rev. D* 60 (1999), p. 113006. arXiv: hep-ph/9905386 [hep-ph].

[11] J. M. Campbell and R. K. Ellis. "t$\bar{t}$ W production and decay at NLO." In: *JHEP* 1207 (2012), p. 052. arXiv: 1204.5678 [hep-ph].

[12] J. M. Campbell, R. K. Ellis, and C. Williams. "Vector boson pair production at the LHC." In: *JHEP* 1107 (2011), p. 018. arXiv: `1105.0020 [hep-ph]`.

[13] S. Catani and M. Grazzini. "An NNLO subtraction formalism in hadron collisions and its application to Higgs boson production at the LHC." In: *Phys. Rev. Lett.* 98 (2007), p. 222002. arXiv: `hep-ph/0703012 [hep-ph]`.

[14] S. Catani, L. Cieri, G. Ferrera, D. de Florian, and M. Grazzini. "Vector boson production at hadron colliders: a fully exclusive QCD calculation at NNLO." In: *Phys. Rev. Lett.* 103 (2009), p. 082001. arXiv: `0903.2120 [hep-ph]`.

[15] M. Czakon, P. Fiedler, and A. Mitov. "Total Top-Quark Pair-Production Cross Section at Hadron Colliders Through $O(\alpha_s^4)$." In: *Phys. Rev. Lett.* 110 (2013), p. 252004. arXiv: `1303.6254 [hep-ph]`.

[16] M. Czakon and A. Mitov. "Top++: A Program for the Calculation of the Top-Pair Cross-Section at Hadron Colliders." In: *Comput. Phys. Commun.* 185 (2014), p. 2930. DOI: `10.1016/j.cpc.2014.06.021`. arXiv: `1112.5675 [hep-ph]`.

[17] D. Galbraith.

[18] M. V. Garzelli, A. Kardos, C. G. Papadopoulos, and Z. Trocsanyi. "t t̄ W^{+-} and t t̄ Z Hadroproduction at NLO accuracy in QCD with Parton Shower and Hadronization effects." In: *JHEP* 11 (2012), p. 056. DOI: `10.1007/JHEP11(2012)056`. arXiv: `1208.2665 [hep-ph]`.

[19] N. Kidonakis. "Two-loop soft anomalous dimensions for single top quark associated production with a W^- or H^-." In: *Phys. Rev. D* 82 (2010), p. 054018. DOI: `10.1103/PhysRevD.82.054018`. arXiv: `1005.4451 [hep-ph]`.

[20] A. Lazopoulos, T. McElmurry, K. Melnikov, and F. Petriello. "Next-to-leading order QCD corrections to t̄tZ production at the LHC." In: *Phys. Lett. B* 666 (2008), p. 62. arXiv: `0804.2220 [hep-ph]`.